Published in final edited form as:
Paris, G., Klinkusch, A., Heidepriem, J., Tsouka, A., Zhang, J., Mende, M., et al. (2020). Laser-induced forward transfer of soft material nanolayers with millisecond pulses shows contact-based material deposition. Applied Surface Science, 508: 144973. doi:10.1016/j.apsusc.2019.144973.

Laser-induced forward transfer of soft material nanolayers with millisecond pulses shows contact-based material deposition

Grigori Paris, Andreas Klinkusch, Jasmin Heidepriem, Alexandra Tsouka, Junfang Zhang, Marco Mende,
Daniela Mattes, Dario Mager, Hans Riegler, Stephan Eickelmann, and Felix F. Loeffler

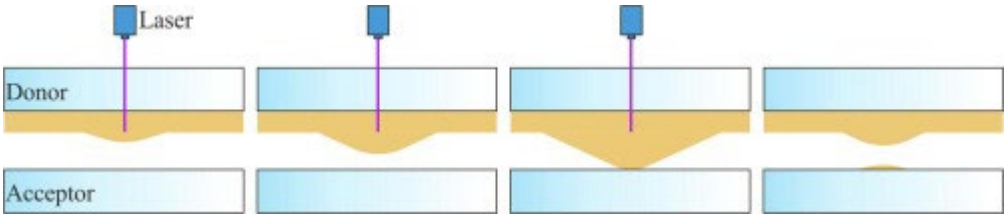

Keywords: High-speed imaging; Experimental and numerical prediction; OpenFOAM; Fluorescence imaging; Vertical scanning interferometry

Laser-induced forward transfer of soft material nanolayers with millisecond pulses shows contact-based material deposition

Authors:

Grigori Paris[a,b], Andreas Klinkusch[c], Jasmin Heidepriem[a], Alexandra Tsouka[a], Junfang Zhang[a], Marco Mende[a], Daniela Mattes[c], Dario Mager[c], Hans Riegler[d], Stephan Eickelmann[a,*] and Felix F. Loeffler[a,*]

Affiliations:

[a]Max Planck Institute of Colloids and Interfaces, Department of Biomolecular Systems, Am Muehlenberg 1, 14476 Potsdam, Germany

[b]Technical University of Berlin, Institute for Mechanics, Department of System Dynamics and Friction Physics, Strasse des 17. Juni 135, 10623 Berlin, Germany

[c]Karlsruhe Institute of Technology, Institute of Microstructure Technology, Hermann-von-Helmholtz-Platz 1, 76344 Eggenstein-Leopoldshafen, Germany

[d]Max Planck Institute of Colloids and Interfaces, Department of Theory & Bio-Systems, Am Muehlenberg 1, 14476 Potsdam, Germany

[*]**Corresponding authors**:

Felix F. Loeffler – felix.loeffler@mpikg.mpg.de

Stephan Eickelmann – stephan.eickelmann@mpikg.mpg.de

Abstract

In this work, we present a qualitative and quantitative experimental analysis, as well as a numerical model, of a novel variant of the laser-induced forward transfer, which uses millisecond laser pulses.

In this process, soft material nanolayer spots are transferred from a donor slide, which is coated with the soft material layer, to an acceptor slide via laser irradiation. This method offers a highly flexible material transfer to perform high-throughput combinatorial chemistry for the generation of biomolecule arrays.

For the first time, we show visual evidence that the main transfer mechanism is contact-based, due to thermal surface expansion of the donor layer. Thus, the process is different from the many known variants of laser-induced forward transfer. We will characterize the maximum axial surface expansion in relation to laser power and pulse duration. On this basis, we derive a numerical model that approximates the axial surface expansion within measurement tolerances. Finally, we analyze the topology of the transferred soft material nanolayer spots by fluorescence imaging and vertical scanning interferometry to determine width, height, and shape of the transferred material. Concluding

from this experimental and numerical data, we can now predict the amount of transferred material in this process.

Keywords: high-speed imaging, experimental and numerical prediction, OpenFOAM, fluorescence imaging, vertical scanning interferometry

1 Introduction

Laser-induced forward transfer (LIFT) is a versatile method for precise and minute amount material deposition, initially introduced in the 1980s for the printing of copper or silver metal films and patterns [1, 2]. Meanwhile, the LIFT process and its variants are established methods enabling precise high-throughput and minute amount material transfer in a variety of fields: Within the field of metallurgy [3, 4, 5, 6] mainly ultrashort laser pulses (nano- to femtosecond) are used, which interact with the donor substrate. These pulses cause material blow off [7, 8, 9] to deposit material through a distance, which is triggered by a shockwave [10, 11].

However, fragile materials that decompose or alter if melted or vaporized, could not be used with the original LIFT conditions for metals. Therefore, Piqué *et al.* [12] proposed the matrix-assisted pulsed laser evaporation-direct write, where the transfer material is embedded in a laser absorbing material *e.g.* polymers. A direct evolution of this is the use of fluids as embedding materials, enabling viable conditions for cell [13, 14] or biomolecule [15, 16, 17] transfer and protect them from the laser-induced heat. The change to a fluid required a radically different setup with special laser transfer parameters and gap sizes between acceptor and donor slide. The usual principle to transfer fluids via LIFT is as follows: A vapor bubble is rapidly expanding due to laser irradiation, pushing the fluid forward. When the bubble starts collapsing, a jet develops, which continues to move forward in axial direction until it reaches the acceptor, resulting in a droplet deposition [18, 19, 20].

Another mode to transfer sensitive materials is the dynamic release layer LIFT [21], where a sacrificial layer absorbs the laser energy and drives the material transfer. Due to their compatibility to a variety of materials, sacrificial metal layers (Au, Cr) [22, 23] can be used to transfer polymers for example. However, metal contamination from the ablation of the metal limits its applicability, which subsequently led to the development of polymeric sacrificial layers. Main examples are the triazene polymer (TP) [24] and blister actuated (BA) LIFT [25], which gave rise to multiple transfer principles: In the case of TP-LIFT, deposition of solid or liquid films over a short distance occurs due to the decomposition of the TP layer by laser ablation [26], which allows for the creation of pixel precise polymer patterns [27] and organic light-emitting diodes [28]. In BA-LIFT, which is usually used to transfer liquid films, a blister in the sacrificial polyimide layer forms, which induces a jet of the fluid towards the acceptor surface [29]. This method was used to manufacture light-emitting diodes [30] and biosensors [31].

Recently, other variants of LIFT emerged, *e.g.* laser-induced backwards transfer (LIBT) [32] and combinatorial laser-induced forward transfer (cLIFT, see Figure 1) [33]. In particular, differently from most LIFT processes, the cLIFT method is based on a diode laser with pulses in the millisecond range, which is considered to be a quasi-continuous wave. Specifically, in contrast to the closely related BA-LIFT [25, 29] a thicker (25 μm) sacrificial polyimide layer and instead of a fluid thin film, an embedding polymer thin film with a chemical building block (*e.g.* activated amino acids), which prevents the building block from decomposition (or reaction with moisture

or dioxygen) and increases the half-life to many months instead of minutes (*e.g.* half-life of activated arginine in solution is 30 min). Additionally, since the polymer thin film is solid at room temperature, it can be placed in direct contact ($\leq$ 10 μm distance) with the acceptor. Furthermore, the transfer of the chemical building block is mild enough (millisecond range), so no chemical reaction takes place. This allows for an activation on demand. Thus, cLIFT is an optimal method for the generation of microarrays, such as peptide [33] and peptoid [34] arrays. Peptide microarrays have a wide range of applications [35], but are especially useful in vaccine research for antibody epitope mapping, *e.g.* in malaria [36, 37]. Finally, we have recently shown that cLIFT only requires a simple diode laser and positioning system to build a cLIFT system for less than 200 € [38].

As in all LIFT methods, within the cLIFT method a donor slide has to be prepared: First, a microscope glass slide is covered with a self-adhesive polyimide foil and, then, spin coated with a polymer matrix, which can be embedded with different chemical building blocks. This donor slide is placed directly on top of an acceptor slide (see Figure 1). Next, through laser irradiation, the polymer matrix is transferred from the donor to the acceptor in very high spot densities (> 10 000 spots per cm^2), enabling the synthesis of peptides and peptoids [34] in high-throughput. To perform experiments with even higher throughput, *e.g.* for proteomics, where hundred thousands of different biomolecules are required, much higher printing resolutions are necessary. Therefore, it is critical to understand the fundamental cLIFT process and its underlying transfer mechanism in detail.

Since the cLIFT method was only recently developed [33], the fundamental transfer mechanism was not yet understood in detail. Thus, different mechanisms are proposed, which may govern this material transfer. In Figure 2b and 2c, two main LIFT mechanisms are described: The first mechanism relies on the ablation or desorption of material from the donor slide (see Figure 2b). The second proposed mechanism is based on thermal deformation, causing direct contact with the acceptor surface and transfer of the donor material (see Figure 2c). Up to date, our specific cLIFT process has not been analyzed in detail with high-speed imaging. Thus, previous experiments lead to the perception that the main characteristic of the transfer is caused by ablation, generating an aerosol, which is transferred [39].

Therefore, in this work, we experimentally studied the cLIFT method in detail with a high-speed camera. We demonstrated for the first time, that, due to blister formation, the main transfer characteristic is a result of a physical contact between acceptor and donor, similar to the contact writing process in a typewriter. This is fundamentally different to the typical LIFT processes, where material is ejected from the donor after for example blister formation [29]. Next, we present a numerical model based on all available data of the polyimide supplier [40] that approximates the process within measurement tolerances and is based on an open-source CFD framework (OpenFOAM). Subsequently, we analyze the experimental free surface expansion in an artificially constructed confined gap and correlate it with the material deposition. Finally, we compare the free surface expansion to our numerical model and state model limitations and future directions.

Here, for the first time, we describe and numerically simulate the cLIFT process, employing millisecond laser pulses (*i.e.* continuous wave laser). Exploiting this knowledge, we can now predict the process and define optimum parameters for an efficient combinatorial material transfer for the production of high-density biomolecule arrays (*e.g.* peptide microarrays).

Nomenclature

α_i	phase fractions		c_{v1}	specific heat capacity polyimide	1.07 J/(g · K)
β	expansion coefficient	$10.2 \cdot 10^{-5}$ 1/K	c_{v2}	specific heat capacity air	0.718 J/(g · K)
γ	absorption coefficient	1003 1/cm	E	total energy	
κ	thermal conductivity		g	gravity	9.81 m/s^2
κ_1	thermal conductivity polyimide	0.12 W/(m · K)	h	polyimide thickness	25 μm
κ_2	thermal conductivity air	0.0262 W/(m · K)	I	identity tensor	
μ	viscosity		M	molar mass polyimide	500 g/mol
μ_1	viscosity polyimide	section 3.1	P	laser power	
μ_2	viscosity air	$1.84 \cdot 10^{-5}$ Pa · s	p	pressure	
μ_l	lower viscosity limit	5 Pa · s	Q	heat source	
μ_u	upper viscosity limit	25 Pa · s	R	reflectivity	0.0439
$\otimes$	outer product of two vectors		R_s	specific gas constant	0.288 J/(g · K)
ψ_i	phase compressibility		T	temperature	
ρ	density		T_0	ambient temperature	296.15 K
ρ_i	phase densities		T_g	glass transition temperature	658.15 K
$\rho_{1,0}$	initial polyimide density	1.42 g/cm^3	T_S	induced laser temperature	section 3.2
τ	deviatoric stress tensor		T_s	surface temperature	section 3.2
b_i	boundaries		u	velocity	
c_1	numerical constant	$9 \cdot 10^{-3}$ 1/K	u_i	phase velocities	
c_2	numerical constant	$4 \cdot 10^{-7}$ 1/K^2	u_r	relative velocity	
c_v	specific heat capacity		X	normed horizontal coordinate	

2 Materials and methods

2.1 Donor slide preparation and cLIFT process

First, a microscope glass is covered with a self-adhesive polyimide foil and flattened with a laminator (see Figure 1a), generating our blank donor slide. Next, a polymer is spin-coated onto the blank donor, creating a process-ready donor slide (see Figure 1b). Then, the donor slide is placed in direct contact with an acceptor slide, resulting in a maximum gap distance between the slides of below 10 μm (gap only due to natural surface roughness). Finally, to generate differently sized spot patterns, the lasing parameters can be varied in lasing duration and power (see Figure 1c).

Within the following investigations standard microscope glass slides were used as acceptors. For the preparation of blank donor slides, normal microscope glass slides were covered with self-adhesive polyimide foil (Kapton HN, DuPont, USA; CMC Klebetechnik GmbH, Germany; 25 μm approximate thickness of polyimide and 45 μm of the adhesive siloxane layer). Therefore, the polyimide foil is placed on top of the microscope glass and flattened with a laminator (see Figure 1a) to ensure optimum adhesion. Then, two solutions were prepared: (1) 18 mg styrene acrylic copolymer (SLEC PLT 7552, Sekisui Chemical GmbH, Germany) in 450 μL dichloromethane (DCM) and 50 μL of 0.01 mg/mL Rhodamine 6G (Rhodamine 6G; Chemodex Ltd., Switzerland) in *N*,*N*-dimethylformamide (DMF) and (2) 150 mg SLEC in 900 μL DCM and 100 μL of 0.01 mg/mL Rhodamine 6G in DCM. The mixtures were spin-coated with 80 rps [41] on separate covered glass slides, obtaining two different types of donor slides without the inclusion of the blank one. Thereby, we obtain donor slides that have a transparent microscope glass as solid support and a laser absorbing polyimide foil with a transparent (non-absorbing) siloxane glue layer. Finally, the spin-coated material on top of the polyimide foil is transferred.

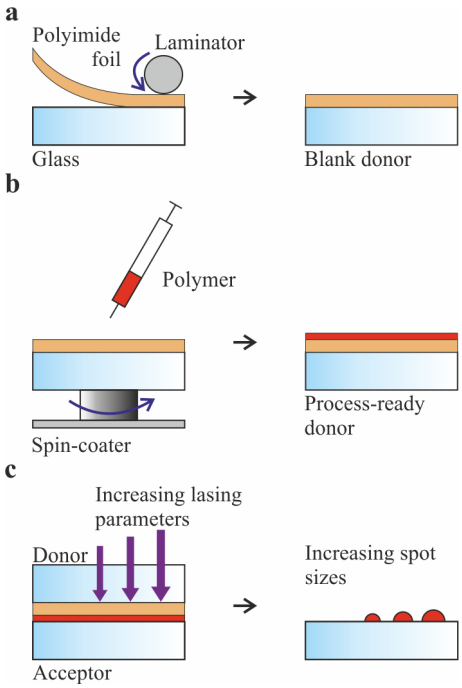

Figure 1: Illustration of the cLIFT process procedure: (a) A blank donor slide is created by attaching a polyimide foil on top of a microscope glass slide and flattening with a laminator. (b) Next, by spin-coating a polymer (or a mixture of polymer and biomolecule) on top of the blank donor slide, a process-ready donor slide is created. (c) Finally, through varying lasing parameters, differently sized spot patterns can be created.

2.2 Lasing setup

A complete description of the used lasing setup is available in [42]. In brief, the lasing system contains a 405 nm wavelength laser, which has a Gaussian beam profile of up to 300 mW power (iBeam smart 405-S, TOPTICA Photonics AG, Germany) that is coupled to a laser scanning system (intelliSCAN III 10, SCANLAB, Germany), equipped with an F-Theta-lens (JENar 170-355-140, JENOPTIK Optical Systems GmbH, Germany). This setup gives a precise planar focus plane and allows for a reproducible and robust laser-induced forward transfer via laser irradiation with highest absorption within the polyimide film of the donor slide [43].

2.3 High-speed imaging

For all experiments, the time dependent surface evolution (general measurement setup see Figure 2) was measured with a PHANTOM V210 high-speed camera (Vision Research, USA). A field of view of 304x128 pixels with a spatial resolution of 1 pixel = 2.2 μm was chosen to have a uniform image size, which captures the surface evolution regardless of the lasing parameters. Furthermore, all experiments were recorded with 39k fps, corresponding to a time resolution of $\Delta t = 2.6 \cdot 10^{-4}$ s. Finally, background subtraction and brightness adjustment were carried out with ImageJ [44] to enable further analysis with Python.

2.4 Fluorescence imaging

Fluorescence images were acquired through the Genepix 4000B (Molecular Devices, USA) scanner with a 5 μm resolution at 532 nm wavelength. If not stated otherwise, all images were evaluated with 33 % laser power and a photo multiplier gain (PMT) of 600.

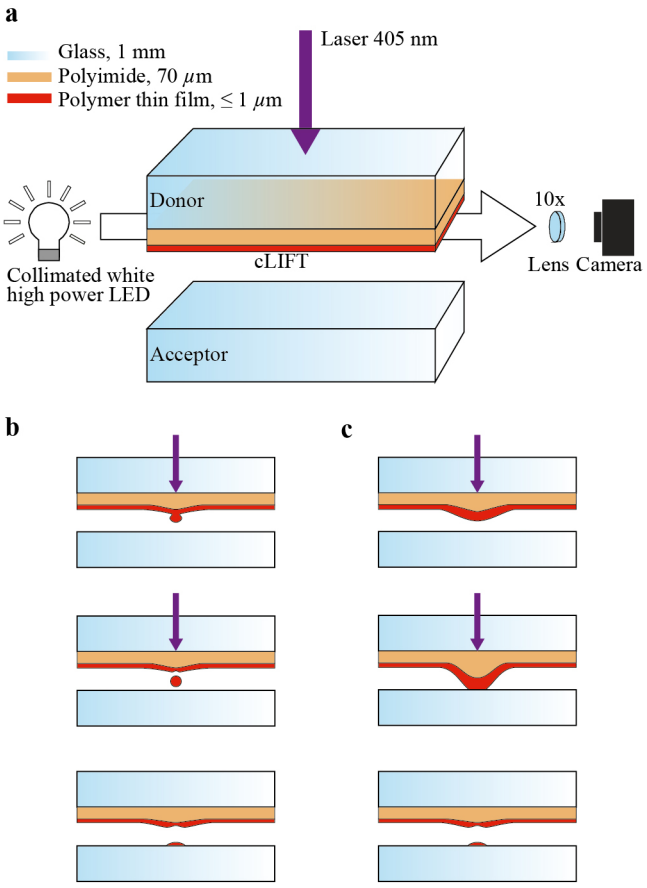

Figure 2: (a) Scheme of the high-speed imaging setup: The donor is placed on top of the acceptor with a spacer in between. A light source illuminates the gap between acceptor and donor. During laser irradiation, the camera, with a 10x magnification, captures the surface evolution of the donor slide within the gap with 39k fps. Two hypothetical main LIFT mechanisms are shown: (b) The first mechanism relies on the ablation or desorption of material from the donor slide, (c) the second is based on thermal deformation, causing direct contact with the acceptor surface and transfer of the donor material.

2.5 Vertical scanning interferometry (VSI)

Vertical scanning interferometry (VSI) measurements were carried out with the Contour GT-KOX-14-157 by Bruker. If not stated otherwise, all measurements were taken with a lateral resolution of 1.351 μm and a 5x magnification lens.

2.6 OpenFOAM

Numerical modeling was carried out with the open-source multiphysics framework OpenFOAM, which is based on the finite volume method. In particular, the *compressibleInterFoam* solver that allows the simulation of compressible flow with two separate phases via the volume of fluid method (VoF) was used to model the cLIFT process as a multiphase flow, which is explained in detail in Section 3.

3 Theory/Calculations

3.1 Governing equations

As stated in Section 2.6, the numerical modeling and analysis was carried out with the *compressibleInterFoam* solver provided by OpenFOAM. Within this solver, the VoF method is used to simulate two compressible, immiscible, and non-isothermal fluids. Furthermore, like many solvers in OpenFOAM, the *compressibleInterFoam* solver is a non-explicitly density based solver, thus the conservation of mass is established via a Poisson type pressure equation and the compressibility is introduced by an equation of state (EOS).

The commonly used set of directly density based compressible multiphase Navier-Stokes equations for density, momentum, total energy, and the phase fraction are as follows (where $\otimes$ is the outer product of two vectors):

$$\begin{cases} \dfrac{\partial \rho}{\partial t} + \nabla \cdot (\rho u) = 0 \\ \dfrac{\partial (\rho u)}{\partial t} + \nabla \cdot (\rho u \otimes u) = -\nabla p + \nabla \cdot \tau + \rho g \\ \dfrac{\partial (\rho E)}{\partial t} + \nabla \cdot (\rho E u) = -\nabla \cdot (p u) + \nabla \cdot (\tau \cdot u) + \nabla \cdot (\kappa \nabla T) + Q \\ \dfrac{\partial (\rho_i \alpha_i)}{\partial t} + \nabla \cdot (\rho_i \alpha_i u_i) = 0 \\ \tau = \mu [\nabla u + (\nabla u)^T - \dfrac{2}{3} I \nabla \cdot u] \\ + \text{initial/boundary conditions (IC/BC), equation of state (EOS)} \end{cases} \tag{1}$$

In contrast in OpenFOAM, as described in [45] and in more detail in [46, 47], the non-directly density based formulation of the *compressibleInterFoam* solver first solves the multiphase tracking equation for one phase

$$\begin{cases} \dfrac{\partial \alpha_1}{\partial t} + \nabla \cdot (\alpha_1 u) + \nabla \cdot (\alpha_1 (1 - \alpha_1) u_r) = \alpha_1 (1 - \alpha_1) \zeta + \alpha_1 \nabla \cdot u \\ u = \alpha_1 u_1 + \alpha_2 u_2, \qquad u_r = u_1 - u_2 \\ \zeta = (\dfrac{\psi_2}{\rho_2} - \dfrac{\psi_1}{\rho_1}) \dfrac{Dp}{Dt}, \qquad \nabla \cdot u = -(\dfrac{\alpha_1 \psi_1}{\rho_1} + \dfrac{\alpha_2 \psi_2}{\rho_2}) \dfrac{Dp}{Dt} \end{cases} \tag{2}$$

and afterwards, limits it through a multi-dimensional limiter for explicit solution (MULES [47]). The artificial compression term $\nabla \cdot (\alpha_1 (1 - \alpha_1) u_r)$, which is only active in the interface zone, is introduced to avoid a blurring out of the interface zone. Hereby, ψ_i represents the compressibility and is introduced within the EOS as

$$\rho_i = \rho_{i,0} + \psi_i p, \qquad \frac{D\rho_i}{Dt} = \psi_i \frac{Dp}{Dt}. \tag{3}$$

In particular, in this work the EOS are

$$\begin{cases} \rho_1 = \rho_{1,0} [1 - \beta (T - T_0)] & \text{for } T \leq T_g \\ \rho_1 = \dfrac{\rho_1 (T_g)}{\sqrt{1 + c_1 (T - T_g)} - c_2 (T - T_g)^2} & \text{for } T > T_g \end{cases} \tag{4}$$

for the polyimide phase, and the ideal gas law $\rho_2 = p/(R_s T)$ for the air phase. With this, the EOS for the polyimide phase is designed to take the known density-temperature relation below T_g into account and induce the expected

pressure gradient after T_g is surpassed. To complete the phase calculation, the air phase is simply calculated via the relation $\alpha_2 = 1 - \alpha_1$.

Then, the momentum and total energy equations

$$\begin{cases} \dfrac{\partial(\rho u)}{\partial t} + \nabla \cdot (\rho u \otimes u) = -\nabla p + \nabla \cdot \tau + \rho g \\ \dfrac{\partial(\rho[c_v T + \frac{1}{2}|u|^2])}{\partial t} + \nabla \cdot (\rho[c_v T + \dfrac{1}{2}|u|^2]u) = -\nabla \cdot (pu) + \nabla \cdot (\kappa \nabla T) \\ \rho = \alpha_1 \rho_1 + \alpha_2 \rho_2, \qquad \mu = \alpha_1 \mu_1 + \alpha_2 \mu_2 \\ \kappa = \alpha_1 \kappa_1 + \alpha_2 \kappa_2, \qquad c_v = \alpha_1 c_{v1} + \alpha_2 c_{v2} \end{cases} \tag{5}$$

are solved. As stated, the pressure of the momentum equation is solved through a Poisson type equation. In specific, a PIMPLE algorithm (a combination of a semi-implicit method for pressure linked equations (SIMPLE) and pressure-implicit with splitting of operators (PISO) algorithm) is used to solve the pressure with 20 outer correctors and 3 inner correctors to account for the high viscosity $\mu_1 = (\mu_u - \mu_l)/(1 + exp(-(T - T_g))) - \mu_l$ and therefore, high stiffness of the polyimide phase. The influence of the surface tension force $\sigma \nabla \cdot (\nabla \alpha_1 / |\nabla \alpha_1|) \nabla \alpha_1$ and the energy change due to shear forces $\nabla \cdot (\tau \cdot u)$ are being neglected, because of their expected minimal influence on the solution. Moreover, a high molecular weight $M = 500$ g/mol was introduced to obtain the relation $c_{p1} \approx c_{v1}$ for the first phase to be conform with OpenFOAM implementation. Finally, this yields the initial boundary value problem (IBVP):

$$\begin{cases} \dfrac{\partial \alpha_1}{\partial t} + \nabla \cdot (\alpha_1 u) + \nabla \cdot (\alpha_1 (1 - \alpha_1) u_r) = \alpha_1 (1 - \alpha_1) \zeta + \alpha_1 \nabla \cdot u \\ \dfrac{\partial(\rho u)}{\partial t} + \nabla \cdot (\rho u \otimes u) = -\nabla p + \nabla \cdot \tau + \rho g \\ \dfrac{\partial(\rho[c_v T + \frac{1}{2}|u|^2])}{\partial t} + \nabla \cdot (\rho[c_v T + \dfrac{1}{2}|u|^2]u) = -\nabla \cdot (pu) + \nabla \cdot (\kappa \nabla T) \\ + \text{IC, BC, EOS} \end{cases} \tag{6}$$

3.2 Simulation setup and boundary conditions

The simulation setup (see Figure 3) consists of a 600 x 75 grid (corresponding to a 400 μm x 75 μm area, rectangular grid boxes) created with the OpenFOAM *blockMesh* utility. Furthermore, the phases are divided into polyimide and air phases, which are set in the *setFields* utility.

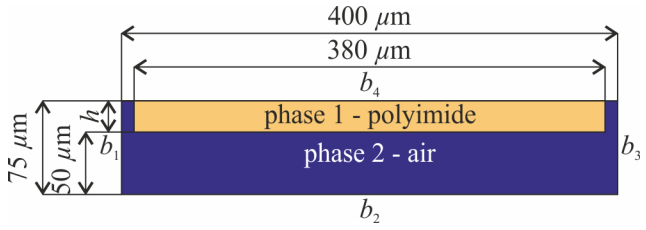

Figure 3: Geometry of the two immiscible phases (polyimide, air) on the 600 x 75 grid (400 μm x 75 μm) with boundaries $b_1 - b_4$.

As we consider the glass slides (acceptor, donor) as adiabatic walls and the sides as open boundaries, the following

set of boundary conditions for α_i, u, p and T apply:

$$\begin{cases} \dfrac{\partial \alpha_i}{\partial n} = 0, \quad \dfrac{\partial p}{\partial n} = 0 & \text{on } b_1, ..., b_4 \\ \dfrac{\partial u}{\partial n} = 0 & \text{on } b_1 \text{ and } b_3 \\ u = 0 & \text{on } b_2 \text{ and } b_4 \\ \dfrac{\partial T}{\partial n} = 0 & \text{on } b_1, b_2 \text{ and } b_3 \end{cases} \tag{7}$$

Only the ideal case of surface heating is considered, since the expected high temperature gradient induced by laser irradiation will establish the volumetric temperature distribution at the beginning of the simulation. Thus, for the induced temperature increase by laser irradiation, the following formulation for a continuous wave laser [48] is taken into account:

$$T_S = T_0 + \frac{P(1-R)}{\pi^{(3/2)}\kappa} \int_0^\infty \frac{exp(-X^2/(u^2+1))}{u^2+1} du \tag{8}$$

By introducing absorption (absorption coefficient extrapolated from [43]) into the system, the actual surface temperature is obtained as

$$T_s = \frac{T_S \int_0^{\Delta z} dz}{\int_0^h exp(-\gamma z) dz} \qquad \text{on } b_4, \tag{9}$$

which is the approximated surface temperature, considering a Beer-Lambert absorption distribution. Finally, physical parameters are taken from the material data sheet [40] if available and the IC are set as $p = 10^5$ Pa, $u = 0$ $\frac{\text{m}}{\text{s}}$, $T = 296.15$ K and α_i as seen in Figure 3 for the entire domain.

4 Results and discussion

4.1 Qualitative process analysis

First, the influence of an artificially introduced distance (gap) between acceptor and donor and a shift of the laser focus plane (changing the laser focus diameter from ∼60 μm to ∼72 μm) were investigated by introducing spacers between and/or under the acceptor (see Figure 4), to obtain a basic characterization of the process. Therefore, spots from two polymer donors coated with 18 mg SLEC, containing a Rhodamine 6G dye (see Section 2.1), were transferred on acceptors (see Figure 4; with 122 mW, 10 ms and 500 μm spot-to-spot distance). Consequently, the increasing distance between acceptor and donor (see Figure 4a) exponentially reduces the measured fluorescence intensity of the deposited material by one order of magnitude from 10^4 to around 10^3 and for a shifting laser focus plane (see Figure 4b) the resulting spots become blurred and larger (from 150 μm to 220 μm). As soon as the distance between acceptor and donor reaches values larger than 70 μm ring like structures with low intensities $< 10^3$ around the main spots occur. Our investigations show that this second order effect only appears, when the contact between the locally expanded donor, due to blister formation, and the acceptor cannot be established (as shown later in Figure 5). Yet, this effect is still under investigation and not fully understood. For a defined high-throughput material deposition, this effect is undesirable and can be avoided by assuring an acceptor-donor distance of less than 70 μm (lasing power 122 mW, lasing duration 10 ms). It should be mentioned that the different

intensities between Figure 4a and 4b for direct contact arise due to the non-optimal alignment of the acceptor to the donor, resulting in an initial non-zero distance between acceptor and donor. Thus, the distance between the acceptor and donor has the largest impact on the process. Finally, the main limitation of the fluorescent imaging approach should be pointed out: The fluorescent dye precisely indicates the position of the deposited material and only qualitatively the amount of deposited material, since the fluorescence intensity does not correlate linearly with the amount of material and seems to stop increasing after reaching a certain material height.

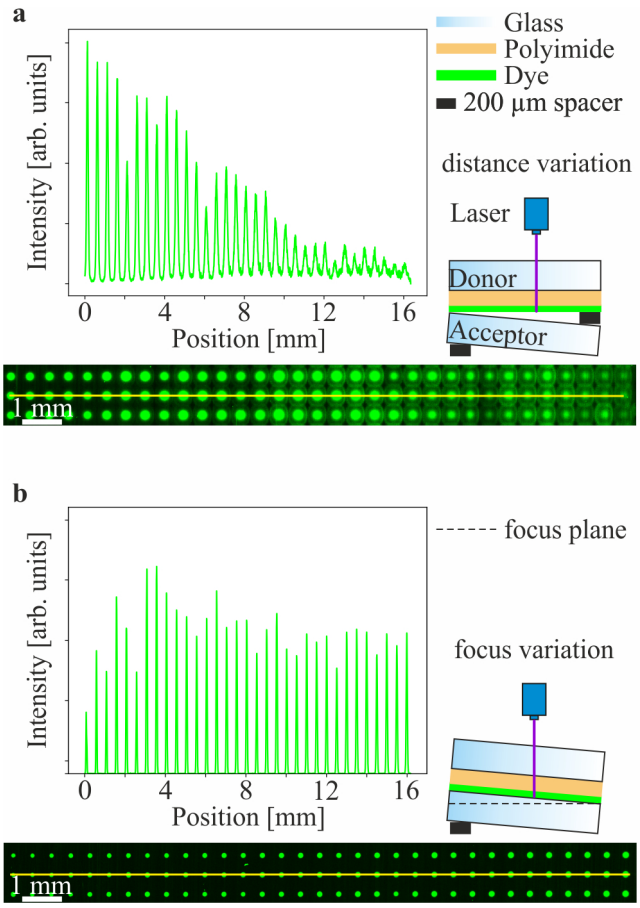

Figure 4: Influence of an artificially introduced distance between acceptor and donor (a, $5 - 200$ μm, lasing power 122 mW, lasing duration 10 ms) as well as a varying focus plane (b, $0 - 200$ μm, 122 mW, 10 ms) on the material deposition scanned with the Genepix 4000B (see Section 2.4): The increasing gap between the acceptor and donor exponentially decreases the measurable fluorescence intensity and introduces a concentric ring like structure for larger gaps. A shift of the focus plane does not significantly influence the fluorescence intensity, but results in blurred material spots.

Next, high-speed imaging experiments were carried out to quantify the previously made observations. To enable an optical detection of the process, light needs to enter the gap. Therefore, small spacers are placed on the sides of the acceptor, allowing light to illuminate the gap. Subsequently, to easily visualize the influence of the laser irradiation on the polyimide surface, we applied extreme lasing parameters (usual transfer parameters ~120 mW for 10 ms). A blank donor (see Section 2.1) was laser irradiated with 210 mW for 100 ms (laser spot diameter ~60 μm) while recoding (see Video 1) the resulting surface expansion from the side (see setup Section 2.3 and results Figure 5). The process can be divided into four parts: (a) Initial laser impact and minor surface deformation in bell shape, (b) linear surface expansion in direction of the normal vector of the surface, (c) contact of the expanded donor with the acceptor, forming a stable structure, and (d) relaxation of the donor surface after the laser is turned off. This

means that the main material deposition occurs due to the contact between the acceptor and donor, neglecting the second order concentric ring structure effect. Furthermore, it could be verified that with the continuous wave laser with millisecond pulses, either no or negligible amount of laser ablation at the donor surface takes place. Thus, the laser mainly acts as precise local heat source within this process.

While imaging the surface expansion of the donor (see top halves of panels in Figure 5), also the mirror image (bottom halves) is visible, allowing for a precise localization of the acceptor surface. Furthermore, a manual evaluation of the surface expansion curve was necessary, due to a rather noisy image output, resulting in a measurement uncertainty of around ±2 pixels, which strongly impacts smaller surface expansions.

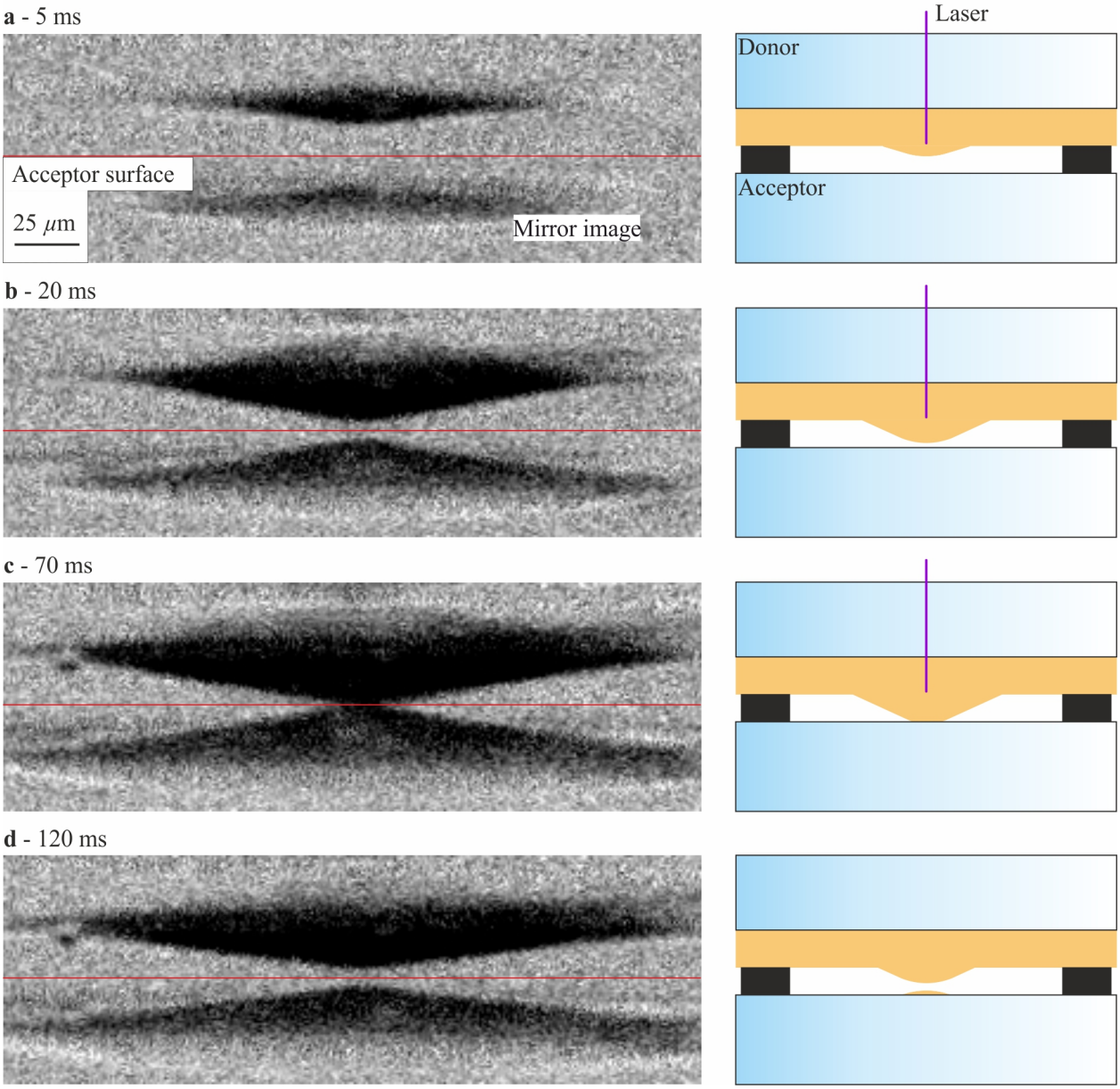

Figure 5: Visualization of the polyimide surface expansion (see Video 1) within the combinatorial laser-induced forward transfer (see Figure 2): For a duration of 100 ms with 210 mW power and a laser spot diameter of ∼60 μm, the polyimide is irradiated with the continuous wave laser (see Section 2.2). The process can be divided into four parts: (a) first deformation of the polyimide, (b) bell-shape growth of the polyimide, (c) contact with the acceptor, and (d) relaxation of the polyimide. Note: The top halves of the images always show the actual polyimide expansion and the bottom halves the reflection (mirror image). This allows for a precise validation of the measurement and helps to identify the acceptor surface according to the symmetry plane (red line).

To understand the impact of each physical property of the polyimide on the transfer process, we established a

numerical model (see Section 3) that can predict the maximum height of the surface expansion. Currently, as shown in Figure 6, our model incorrectly approximates the surface shape. This results from the in reality more complex polyimide structure: The specific polyimide (Kapton, HN, Dupont) is orthotropic, as mentioned in [49, 50], whereas our simulation assumes it as isotropic. As presented by Munoz-Martin *et al.* [51], the laser-induced forward transfer of a more isotropic silver paste shows the modelled linear spherical expansion shape. Nevertheless, one expansion direction of an orthotropic material can be approximated through an isotropic model, which allows the prediction of a single representative macroscopic value. Thus, the influence of physical parameters on the maximum surface expansion can be numerically predicted, which in combination with experimental deposition data, allows for a prediction of the transferred material depending on separate physical properties.

The simulation geometry was given a large enough width to reduce boundary effects on the maximum surface expansion and an approximated gap corresponding to the experiment to introduce the influence of the acceptor. Finally, to stabilize the simulation, the polyimide was cut before the boundaries, which does not affect the maximum surface expansion.

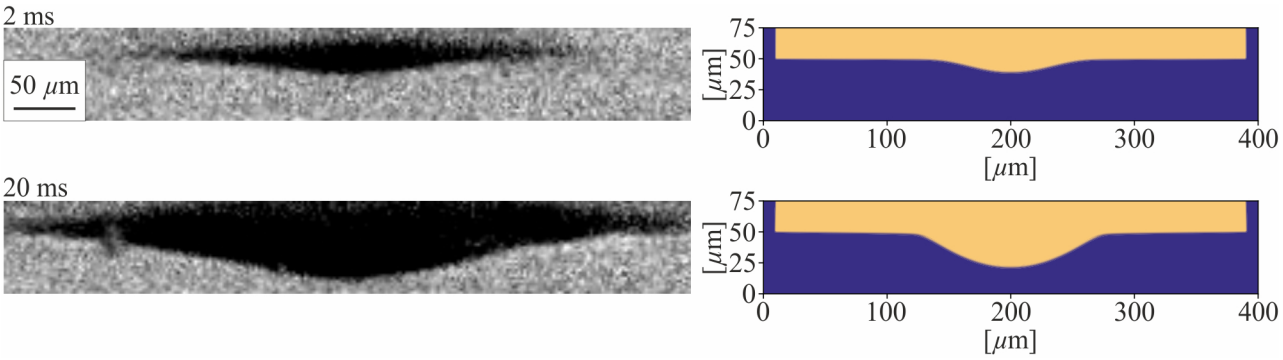

Figure 6: Comparison of experimental and numerical results: The shape of the experimental free surface expansion shows a large ratio between the expanded width and height, compared to the almost spherical expansion of the simulated case after 2 and 20 ms laser irradiation with 210 mW. This is likely caused by the orthotropic nature of the polyimide, which is assumed as isotropic within the simulation. Yet, the maximum surface amplitudes in both cases are within measurement error.

4.2 Quantitative analysis of the donor surface expansion

The experimental data (see Figure 7) shows that for all used laser powers ($60 - 210$ mW) within the timeframe of 20 ms laser irradiation, the maximum surface height expands logarithmically and relaxes exponentially. Furthermore, it is apparent that a larger laser power increases the maximum surface height due to the increased thermal energy. Next, it is evident that the polyimide keeps a plastic deformation even after completely cooling down, which can be larger than 10 μm, whereas the gap within a normal transfer regime is below 10 μm (see Section 2.1). In that case, the donor is tilted due to this local deformation, which results in imprecise and blurred following transfers. Thus, to have a more reliable prediction, a minimization of the plastic deformation is desirable. In a previous work [42], material deposition with laser powers below 60 mW have been observed, although we cannot detect surface expansions for those powers. Thus, for laser powers below the 60 mW threshold, it is assumed that only a minimal surface expansion occurs and a negligible amount of plastic deformation takes place, resulting in an almost completely reversible process. Hence, the most robust and reproducible material transfer occurs for lower

laser powers, which will be investigated in future experiments.

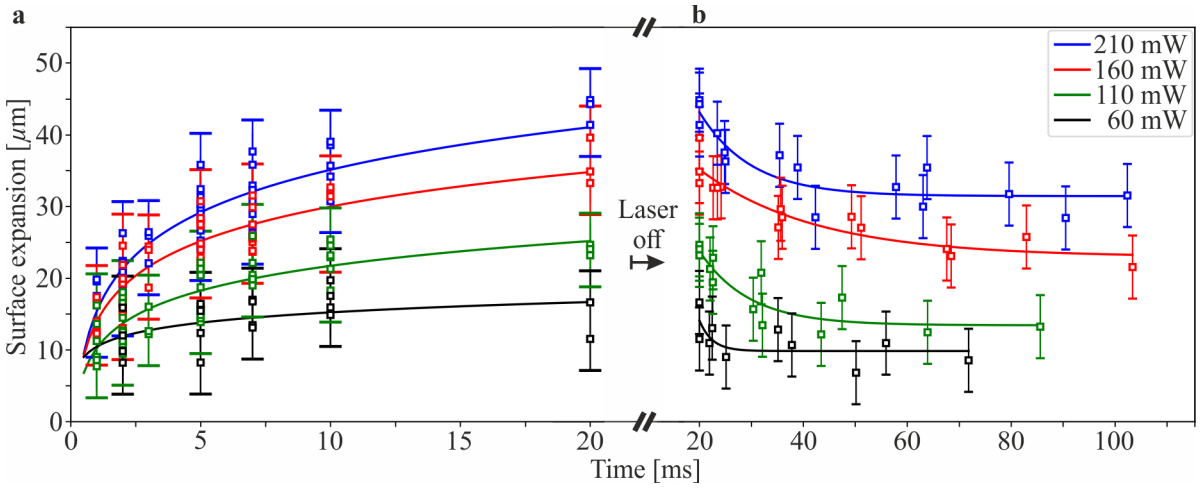

Figure 7: Experimental measurement results for a laser irradiation duration of 20 ms with four different power settings (60, 110, 160 and 210 mW): For each data point, a tolerance of ±2 pixels corresponding to ±4.4 μm, is taken into account, because of the manual evaluation process. A logarithmic (a) and exponential (b) fit is used to describe the polyimide surface growth and relaxation respectively. Finally, with increasing power, a larger surface expansion and irreversible plastic deformation can be observed.

For the comparison between the experimental and deterministic numerical results, we took, if available, all physical parameters from the material data sheet [40] or measurement values. Despite some differences between the experimental fit and the numerical prediction, all results lie within the measurement tolerance of ±2 pixels, corresponding to ±4.4 μm. In comparison to the experimental fit, the numerical surface expansions show root shape growths, which converge to the lower limit of the experimental data sets. This can be explained by the implemented EOS (see Equation 4), which converges with a square root and does not account for plastic deformation. A collaps of the model for 60 mW laser power with almost zero surface expansion was observed and, therefore, was not included in Figure 8a. is a result of the implemented EOS, which introduces a density drop and thus a moving pressure wave from the boundary b_4, after laser irradiation. For the case of 60 mW laser power, the pressure wave almost vanishes before reaching the surface, yielding close to 0 μm surface expansion. For all other cases, after 5 ms, a negligible deviation of less than 2 pixels = 4.4 μm (within measurement tolerance) between the experimental fit and numerical simulation can be observed. Below 5 ms, the maximum surface expansion slightly deviates from the prediction (up to 3.5 pixels), which again results from the pressure wave that needs time to move through the polyimide to influence the surface.

With this validated numerical model, we can now predict the dynamic behavior of the blister formation and the influence of individual physical parameters. Furthermore, we can derive the heat distribution within the polyimide layer and minimize the effect of spatially and temporally adjacent blister formations on each other.

4.3 Material deposition topology

The topology of the material deposition is analyzed through fluorescence imaging and vertical scanning interferometry (VSI). To compare both methods with each other four samples have been prepared (two blank and two 150 mg SLEC polymer coated donors (see Section 2.1)), which are used for a model transfer to different acceptors in an increasing intensity pattern (see Figure 9).

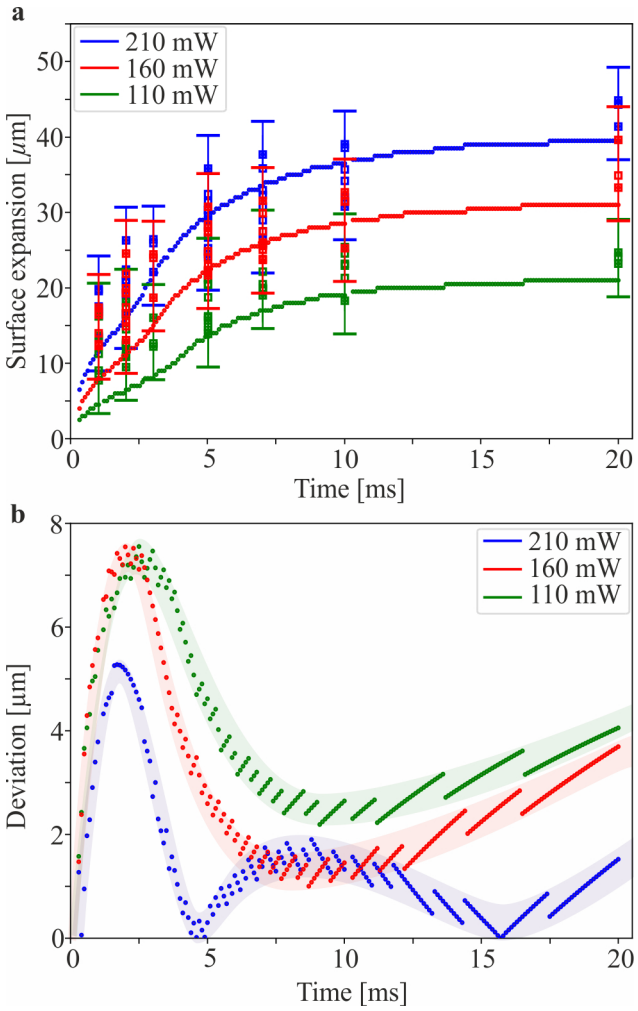

Figure 8: Simulation results for a laser irradiation duration of 20 ms (a), showing the maximum surface expansion for all lasing durations for up to 20 ms with three different power settings (110, 160 and 210 mW) and deviation from the experimental fit (b, also see Figure 7). The numerical results show root shape growth with generally small deviation ± 4.4 μm from the experimental data fit. However, the starting deviation is slightly above this threshold. Finally, the convergence value of the experiment and simulation differ, since the deviation increases again after $12 - 15.5$ ms. Due to simulation effects, data shows some discontinuous behavior.

Since the blank donor did neither contain a polymer coating, nor a fluorescent dye, the fluorescence of only the transferred polyimide itself can be detected (see Figure 9a). Yet, because the amount of transferred polyimide is so little, the fluorescence imaging settings had to be raised to maximum settings. Subsequently, we observed that the transfer from a blank donor results in a barely visible spot deposition pattern (spots up to 240 μm in diameter). Generally, the resulting spot widths from VSI measurements (see Figure 9b) coincide with the fluorescence measurements within 10 % error. Although polyimide is known to posses fluorescent properties, the weak fluorescence signal (low signal to noise ratio) can be explained by the extremely thin layers of small transferred amounts, showing material deposition heights of less than 1 nm from the blank polyimide donor for very high laser energies. Thus, we conclude that the transfer of polyimide may be neglected.

After transferring from the 150 mg SLEC donor under normal transfer conditions (see Section 2.1, donor and acceptor slides in direct contact), containing the Rhodamine 6G dye, a clear and sharp transfer pattern (see Figure 9c) is observed through fluorescence imaging with spot widths of up to 165 μm. The VSI measurement of an equivalent sample (see Figure 9d) shows that the measured width of the fluorescence imaging corresponds to the

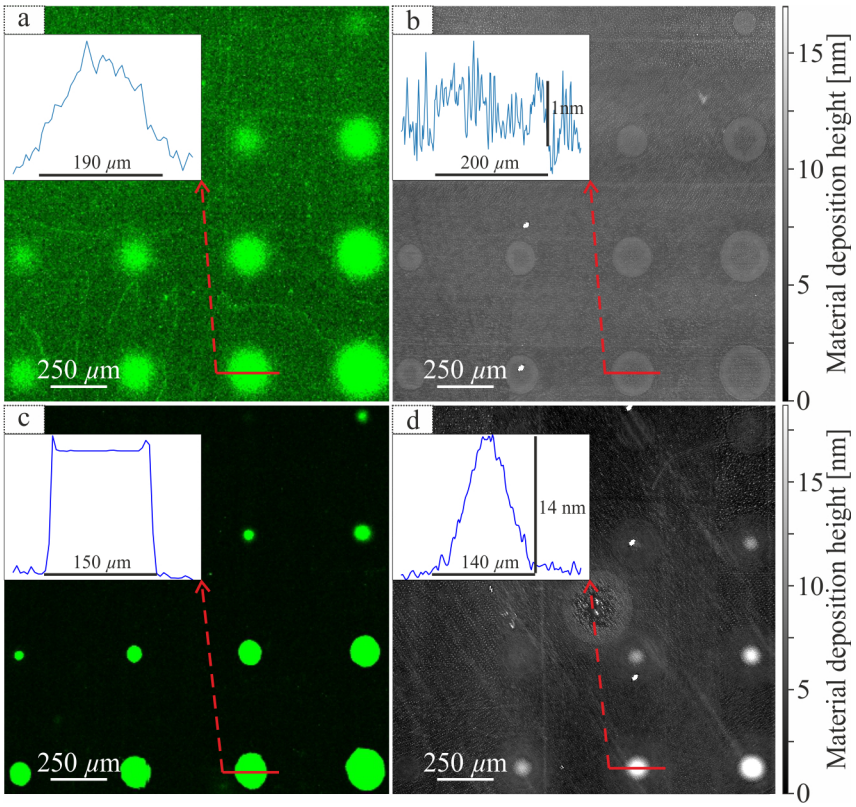

Figure 9: Fluorescence and VSI measurement of blank and 150 mg SLEC coated donors (see Section 2.1) with $60 - 210$ mW lasing power (linearly spaced, top to bottom) and 5, 7, 10, 20 ms lasing duration (left to right): Fluorescence imaging of the blank donor (Figure 9a) was evaluated with 100 % laser power and 1000 PMT (see Section 2.4). Within the measurement of the two different samples (Figure 9a and 9b) a similar transfer spot width is observed with a maximum difference of 10 %. Furthermore, the VSI measurement in Figure 9b shows that the height of transferred polyimide from a blank donor is smaller than 1 nm.
Fluorescence imaging of the donor coated with 150 mg SLEC containing the dye Rhodamine 6G (see Figure 9c), shows a more prominent and sharp transfer, compared to the VSI measurement sample. Yet, the width of the transferred spots is comparable (maximum difference below 10 %), when considering the first rising signal above 1 nm as the maximum width. Thus, the range for the transfer height lies between $0.5 - 15.5$ nm.

real width, with a deviation of up to 10 %. Therefore, we consider the beginning of a spot, when the signal rises above 1 nm deposition height. For example, the transfer of only polyimide from a blank donor slide with 160 mW lasing power and 10 ms lasing duration is shown in Figure 9b. Finally, bell shaped material deposition distributions with heights of up to 15.5 nm can be observed.

For our purposes, the main parameter of interest is the material deposition width, to eventually reach higher spot densities. As mentioned before, the fluorescence intensity does not linearly correlate with the height of the transferred material. Yet, the quantitative analysis of fluorescence imaging data sufficiently resembles the expected spot width. Therefore, a parameter variation of 60, 110, 160 and 210 mW lasing power and $2 - 20$ ms lasing duration (see Figure 10) was used. Then, the material deposition width was evaluated based on a fluorescence intensity threshold, which resulted in different upper width tolerances for the parameters 60, 110, 160 and 210 mW (20, 15, 15, and 20 μm respectively). A general decrease in spot width is observed in both, lower lasing power and lower lasing duration with minimum spot sizes around $60 - 85$ μm width for 60 mW lasing power and 12 ms lasing duration. We generally choose lower lasing parameters, because the material transfer becomes more predictable with a lower donor surface expansion, resulting in smaller spot widths (see Figure 10).

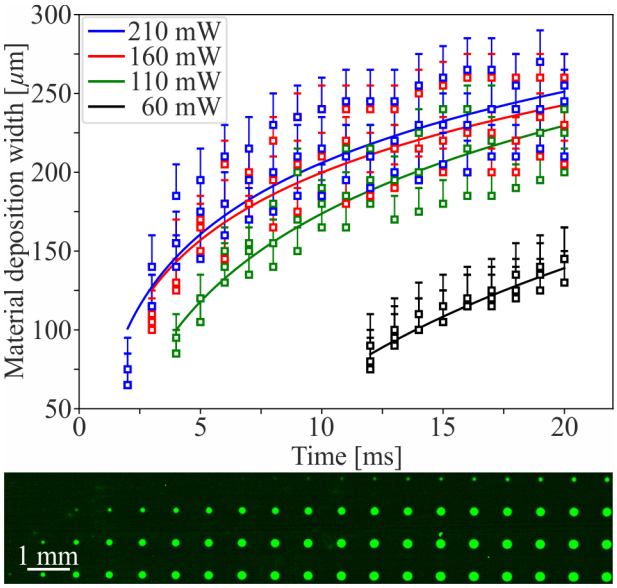

Figure 10: Quantitative analysis of the material deposition width for 60, 110, 160, and 210 mW lasing power (top to bottom) and $2-20$ ms lasing duration (left to right): For each parameter set of 60, 110, 160, and 210 mW, the upper tolerances of 20, 15, 15, and 20 μm respectively are derived from a fluorescence intensity threshold. Next, we logarithmically fitted the data for all power sets, which results in less reliable fitting for large laser powers and long lasing durations. For decreasing lasing powers, we observe a steady reduction of the deposition width (minimum spot width of $60-85$ μm for 60 mW lasing power and 12 ms lasing duration) with higher reproducibility.

5 Conclusion

In this work, we present a quantitative experimental and numerical characterization of the combinatorial laser-induced forward transfer (cLIFT) method, transferring soft material from a donor surface to an acceptor slide. In contrast to other LIFT processes that employ ultrashort pulses to transfer material, we employ millisecond laser pulses.

In initial qualitative experiments we showed that a shift of the focus plane (see Figure 4b) has a negligible influence on the transfer. This is expected, since we do not use a beam expander between the laser source and the scanning system, making the setup more tolerant to height deviations. Next, we presented a setup with an introduced artificial gap between donor and acceptor (see Figure 4a), which reduces the transfer. Then, we visualized the transfer process itself, using high energy lasing conditions, which provided strong evidence that the main transfer mechanism of this method is based on contact between acceptor and donor. Furthermore, we could quantify the maximum surface expansion of the donor (see Figure 7) in regards to lasing power and duration, and we compared it with a numerical model (see Figure 8). Our model accurately predicts the maximum axial surface expansion of a donor surface during the transfer process. Subsequently, we showed VSI measurements (see Figure 9a and 9b) of transferred material and compared it to an identical transfer with a fluorescent dye (see Figure 9c and 9d) to validate that fluorescence imaging can be used to approximate the width (but not height) of transferred polymer material. Finally, fluorescence data of a transferred spot pattern with various lasing parameters was presented (see Figure 10), which indicates minimum spot sizes of $60-85$ μm for 60 mW lasing power and 12 ms lasing duration. This shows that patterns with very high spot densities are possible, which is one of the core goals for future applications, such as high-density microarrays.

As mentioned in Section 4.1, the bell shape of the surface expansion is only approximated, since the polyimide

is considered to be isotropic and not orthotropic within the simulation. So far, we could validate the model only for laser powers above 110 mW. In the future, it should be also validated for the range between $60 - 110$ mW. Additionally, temperature dependency on physical parameters, such as specific heat capacity, thermal conductivity, or reflectivity should be introduced. However, these parameters were not available from the vendor of the polyimide, which would result in very time consuming experiments beyond the scope of this project. Finally, the contact between the surface and the acceptor should be modelled.

In the future, we will investigate the influence of the acceptor wettability on the material transfer, *e.g.* the interaction between the blister of the donor and a hydrophobic or hydrophilic acceptor surface. Therefore, different types of acceptor surfaces will be used, featuring a variety of chemical coatings and their influence on the material deposition. Due to the nanoscale thickness of the transferred material, resulting in high numerical cost, the transfer process itself was not yet modelled.

In summary, based on this work, we have not only shown that the cLIFT process, using simple and cost efficient continuous wave lasers, is actually based on a contact mechanism, but we can also deduce optimized process parameters to minimize spot size and plastic surface deformation, making the cLIFT process more reliable and easy to predict. This will enable an optimized production of high-density microarrays with this novel high-throughput technology.

Author contribution

G. P. performed all experimental and numerical experiments, developed the theoretical approximation of the process, carried out the qualitative and quantitative analysis, and wrote the initial manuscript. A. K. carried out the VSI measurement. J. H., A. T., J. Z., and M. M. supported the laboratory work. D. M. supervised the work of A. K.. D. Mag. assisted with the technical setup. H. R. supported preliminary experiments. S. E. and F. F. L. supervised the project and revised the manuscript.

Declaration of interest

F.F.L. is named on a pending patent application related to laser-based microarray synthesis. All other authors declare no competing interest.

Acknowledgements

We would like to acknowledge Prof. Peter H. Seeberger and the Biomolecular Systems Department, as well as, the Max Planck Society for their support.

Funding

This work was supported by the German Federal Ministry of Education and Research [BMBF, grant number 13XP5050A], the MPG-FhG cooperation [Glyco3Display], and the Max Planck Society.

References

[1] J. Bohandy, B. F. Kim, F. J. Adrian, Metal deposition from a supported metal film using an excimer laser, Journal of Applied Physics 60 (4) (1986) 1538–1539. doi:10.1063/1.337287.

[2] J. Bohandy, B. F. Kim, F. J. Adrian, A. N. Jette, Metal deposition at 532 nm using a laser transfer technique, Journal of Applied Physics 63 (4) (1988) 1158–1162. doi:10.1063/1.340023.

[3] D. A. Willis, V. Grosu, Microdroplet deposition by laser-induced forward transfer, Applied Physics Letters 86 (24) (2005) 244103. doi:10.1063/1.1944895.

[4] I. Zergiotti, S. Mailis, N. Vainos, C. Fotakis, S. Chen, C. Grigoropoulos, Microdeposition of metals by femtosecond excimer laser, Applied Surface Science 127-129 (1998) 601–605. doi:10.1016/s0169-4332(97)00713-7.

[5] I. Zergiotti, S. Mailis, N. Vainos, P. Papakonstantinou, C. Kalpouzos, C. Grigoropoulos, C. Fotakis, Microdeposition of metal and oxide structures using ultrashort laser pulses, Applied Physics A: Materials Science & Processing 66 (5) (1998) 579–582. doi:10.1007/s003390050717.

[6] U. Zywietz, A. B. Evlyukhin, C. Reinhardt, B. N. Chichkov, Laser printing of silicon nanoparticles with resonant optical electric and magnetic responses, Nature Communications 5 (3402) (2014). doi:10.1038/ncomms4402.

[7] V. Schultze, M. Wagner, Blow-off of aluminium films, Applied Physics A Solids and Surfaces 53 (3) (1991) 241–248. doi:10.1007/bf00324259.

[8] Y. Nakata, T. Okada, Time-resolved microscopic imaging of the laser-induced forward transfer process, Applied Physics A: Materials Science & Processing 69 (1 Supplement) (1999) S275–S278. doi:10.1007/s003390051399.

[9] M. Feinaeugle, A. Alloncle, P. Delaporte, C. Sones, R. Eason, Time-resolved shadowgraph imaging of femtosecond laser-induced forward transfer of solid materials, Applied Surface Science 258 (22) (2012) 8475–8483. doi:10.1016/j.apsusc.2012.04.101.

[10] C. Porneala, D. A. Willis, Observation of nanosecond laser-induced phase explosion in aluminum, Applied Physics Letters 89 (21) (2006) 211121. doi:10.1063/1.2393158.

[11] P. Delaporte, A.-P. Alloncle, [INVITED] laser-induced forward transfer: A high resolution additive manufacturing technology, Optics & Laser Technology 78 (2016) 33–41. doi:10.1016/j.optlastec.2015.09.022.

[12] A. Piqué, D. Chrisey, R. Auyeung, J. Fitz-Gerald, H. Wu, R. McGill, S. Lakeou, P. Wu, V. Nguyen, M. Duignan, A novel laser transfer process for direct writing of electronic and sensor materials, Applied Physics A: Materials Science & Processing 69 (1 Supplement) (1999) S279–S284. doi:10.1007/s003390051400.

[13] B. Ringeisen, D. Chrisey, A. Piqué, H. Young, R. Modi, M. Bucaro, J. Jones-Meehan, B. Spargo, Generation of mesoscopic patterns of viable escherichia coli by ambient laser transfer, Biomaterials 23 (1) (2002) 161–166. doi:10.1016/s0142-9612(01)00091-6.

[14] D. Riester, J. Budde, C. Gach, A. Gillner, M. Wehner, High speed photography of laser induced forward transfer (LIFT) of single and double-layered transfer layers for single cell transfer, Journal of Laser Micro/Nanoengineering 11 (2) (2016) 199–203. doi:10.2961/jlmn.2016.02.0010.

[15] B. Ringeisen, P. Wu, H. Kim, A. Pique, R. Auyeung, H. Young, D. Chrisey, D. Krizman, Picoliter-scale protein microarrays by laser direct write, Biotechnology Progress 18 (5) (2002) 1126–1129. doi:10.1021/bp015516g.

[16] P. Serra, M. Colina, J. M. Fernández-Pradas, L. Sevilla, J. L. Morenza, Preparation of functional DNA microarrays through laser-induced forward transfer, Applied Physics Letters 85 (9) (2004) 1639–1641. doi:10.1063/1.1787614.

[17] P. Serra, J. M. Fernández-Pradas, M. Colina, M. Duocastella, J. Domínguez, J. L. Morenza, Laser-induced forward transfer: a direct-writing technique for biosensors preparation, Journal of Laser Micro/Nanoengineering 1 (3) (2006) 236–242. doi:10.2961/jlmn.2006.03.0017.

[18] M. Duocastella, J. M. Fernández-Pradas, P. Serra, J. L. Morenza, Jet formation in the laser forward transfer of liquids, Applied Physics A: Materials Science & Processing 93 (2) (2008) 453–456. doi:10.1007/s00339-008-4781-y.

[19] M. Duocastella, J. M. Fernández-Pradas, J. L. Morenza, P. Serra, Time-resolved imaging of the laser forward transfer of liquids, Journal of Applied Physics 106 (8) (2009) 084907. doi:10.1063/1.3248304.

[20] M. Duocastella, J. Fernández-Pradas, P. S. J.L. Morenza, Sessile droplet formation in the laser-induced forward transfer of liquids: A time-resolved imaging study, Thin Solid Films 518 (18) (2010) 5321–5325. doi:10.1016/j.tsf.2010.03.082.

[21] W. A. Tolbert, I. S. Lee, M. M. Doxtader, E. W. Ellis, D. D. Dlott, High-speed color imaging by laser ablation transfer with a dynamic release layer: fundamental mechanisms, Journal of Imaging Science 37 (4) (1993) 411–421.

[22] J. M. Fitz-Gerald, A. Piqué, D. B. Chrisey, P. D. Rack, M. Zeleznik, R. C. Y. Auyeung, S. Lakeou, Laser direct writing of phosphor screens for high-definition displays, Applied Physics Letters 76 (11) (2000) 1386–1388. doi:10.1063/1.126040.

[23] C. Boutopoulos, V. Tsouti, D. Goustouridis, S. Chatzandroulis, I. Zergiotti, Liquid phase direct laser printing of polymers for chemical sensing applications, Applied Physics Letters 93 (19) (2008) 191109. doi:10.1063/1.3025596.

[24] T. Lippert, A. Wokaun, J. Stebani, O. Nuyken, J. Ihlemann, Triazene polymers designed for excimer laser ablation 206 (1) (1993) 97–110. doi:10.1002/apmc.1993.052060110.

[25] N. T. Kattamis, P. E. Purnick, R. Weiss, C. B. Arnold, Thick film laser induced forward transfer for deposition of thermally and mechanically sensitive materials, Applied Physics Letters 91 (17) (2007) 171120. doi:10.1063/1.2799877.

[26] R. Fardel, M. Nagel, F. Nüesch, T. Lippert, A. Wokaun, Shadowgraphy investigation of laser-induced forward transfer: Front side and back side ablation of the triazene polymer sacrificial layer, Applied Surface Science 255 (10) (2009) 5430–5434. doi:10.1016/j.apsusc.2008.07.187.

[27] V. Dinca, R. Fardel, J. Shaw-Stewart, F. Pietrantonio, D. Cannata, M. Benetti, E. Verona, A. Palla-Papavlu, M. Dinescu, T. Lippert, Laser-induced forward transfer: An approach to single-step polymer microsensor fabrication, Applied Surface Science 8 (3) (2010) 436–440. doi:10.1166/s1.2010.1291.

[28] R. Fardel, M. Nagel, F. Nüesch, T. Lippert, A. Wokaun, Fabrication of organic light-emitting diode pixels by laser-assisted forward transfer, Applied Physics Letters 91 (6) (2007) 061103. doi:10.1063/1.2759475.

[29] M. S. Brown, N. T. Kattamis, C. B. Arnold, Time-resolved study of polyimide absorption layers for blister-actuated laser-induced forward transfer, Journal of Applied Physics 107 (8) (2010) 083103. doi:10.1063/1.3327432.

[30] N. T. Kattamis, N. D. McDaniel, S. Bernhard, C. B. Arnold, Ambient laser direct-write printing of a patterned organo-metallic electroluminescent device, Organic Electronics 12 (7) (2011) 1152–1158. doi:10.1016/j.orgel.2011.03.032.

[31] L. Hecht, K. Rager, M. Davidonis, P. Weber, G. Gauglitz, A. Dietzel, Blister-actuated LIFT printing for multiparametric functionalization of paper-like biosensors, Micromachines 10 (4) (2019) 221. doi:10.3390/mi10040221.

[32] M. Feinaeugle, D. J. Heath, B. Mills, J. A. Grant-Jacob, G. Z. Mashanovich, R. W. Eason, Laser-induced backward transfer of nanoimprinted polymer elements, Applied Physics A 122 (398) (2016). doi:10.1007/s00339-016-9953-6.

[33] F. F. Loeffler, T. C. Foertsch, R. Popov, D. S. Mattes, M. Schlageter, M. Sedlmayr, B. Ridder, F.-X. Dang, C. von Bojničić-Kninski, L. K. Weber, A. Fischer, J. Greifenstein, V. Bykovskaya, I. Buliev, F. R. Bischoff, L. Hahn, M. A. R. Meier, S. Bräse, A. K. Powell, T. S. Balaban, F. Breitling, A. Nesterov-Mueller, High-flexibility combinatorial peptide synthesis with laser-based transfer of monomers in solid matrix material, Nature Communications 7 (11844) (2016). doi:10.1038/ncomms11844.

[34] D. S. Mattes, B. Streit, D. R. Bhandari, J. Greifenstein, T. C. Foertsch, S. W. Münch, B. Ridder, C. v. Bojničić-Kninski, A. Nesterov-Mueller, B. Spengler, U. Schepers, S. Bräse, F. F. Loeffler, F. Breitling, Combinatorial synthesis of peptoid arrays via laser-based stacking of multiple polymer nanolayers, Macromolecular Rapid Communications 40 (6) (2018) 1800533. doi:10.1002/marc.201800533.

[35] L. C. Szymczak, H.-Y. Kuo, M. Mrksich, Peptide arrays: Development and application, Analytical Chemistry 90 (1) (2017) 266–282. doi:10.1021/acs.analchem.7b04380.

[36] J. Tan, B. K. Sack, D. Oyen, I. Zenklusen, L. Piccoli, S. Barbieri, M. Foglierini, C. S. Fregni, J. Marcandalli, S. Jongo, S. Abdulla, L. Perez, G. Corradin, L. Varani, F. Sallusto, B. K. L. Sim, S. L. Hoffman, S. H. I. Kappe, C. Daubenberger, I. A. Wilson, A. Lanzavecchia, A public antibody lineage that potently inhibits

malaria infection through dual binding to the circumsporozoite protein, Nature Medicine 24 (4) (2018) 401–407. doi:10.1038/nm.4513.

[37] T. Jaenisch, K. Heiss, N. Fischer, C. Geiger, F. R. Bischoff, G. Moldenhauer, L. Rychlewski, A. Sié, B. Coulibaly, P. H. Seeberger, L. S. Wyrwicz, F. Breitling, F. F. Loeffler, High-density peptide arrays help to identify linear immunogenic b-cell epitopes in individuals naturally exposed to malaria infection, Molecular & Cellular Proteomics 18 (4) (2019) 642–656. doi:10.1074/mcp.ra118.000992.

[38] S. Eickelmann, A. Tsouka, J. Heidepriem, G. Paris, J. Zhang, V. Molinari, M. Mende, F. F. Loeffler, A low-cost laser-based nano-3d polymer printer for rapid surface patterning and chemical synthesis of peptide and glycan microarrays, Advanced Materials Technologies 4 (11) (2019) 1900503. doi:10.1002/admt.201900503.

[39] T. C. Foertsch, A. T. Davis, R. Popov, C. von Bojničić-Kninski, F. E. Held, S. B. Tsogoeva, F. F. Loeffler, A. Nesterov-Mueller, Spatial modes of laser-induced mass transfer in micro-gaps, Applied Sciences 9 (7) (2019) 1303. doi:10.3390/app9071303.

[40] Kapton, HN, data sheets, last accessed 24.06.2019 16:05.
URL `https://www.dupont.com/products/kapton-hn.html`

[41] J. Danglad-Flores, S. Eickelmann, H. Riegler, Deposition of polymer films by spin casting: A quantitative analysis, Chemical Engineering Science 179 (2018) 257–264. doi:10.1016/j.ces.2018.01.012.

[42] G. Paris, J. Heidepriem, A. Tsouka, M. Mende, S. Eickelmann, F. F. Loeffler, Automated laser-assisted synthesis of microarrays for infectious disease research, Microfluidics, BioMEMS, and Medical Microsystems XVII 10875 (2019). doi:10.1117/12.2516781.

[43] R. French, J. Rodríguez-Parada, M. Yang, R. Derryberry, N. Pfeiffenberger, Optical properties of polymeric materials for concentrator photovoltaic systems, Solar Energy Materials and Solar Cells 95 (8) (2011) 2077–2086. doi:10.1016/j.solmat.2011.02.025.

[44] C. T. Rueden, J. Schindelin, M. C. Hiner, B. E. DeZonia, A. E. Walter, E. T. Arena, K. W. Eliceiri, ImageJ2: ImageJ for the next generation of scientific image data, BMC Bioinformatics 18 (1) (2017). doi:10.1186/s12859-017-1934-z.

[45] M. Jadidi, M. Tembely, S. Moghtadernejad, A. Dolatabadi, Coupled level set and volume of fluid method in openfoam with application to compressible two-phase flow, 22nd Annual Conference of the CFD Society of Canada (2014).

[46] H. Rusche, Computational fluid dynamics of dispersed two-phase flows at high phase fractions, Ph.D. thesis, Imperial College of Science, Technology and Medicine Department of Mechanical Engineering (2002).

[47] S. M. Damián, An extended mixture model for the simultaneous treatment of short and long scale interfaces, Ph.D. thesis, Universidad Nacional del Litoral, Facultad de Ingeniería y Ciencias Hídricas (2013).

[48] J. E. Moody, R. H. Hendel, Temperature profiles induced by a scanning cw laser beam, Journal of Applied Physics 53 (6) (1982) 4364–4371. doi:10.1063/1.331217.

[49] B. F. Blumentritt, Anisotropy and dimensional stability of polyimide films, Polymer Engineering and Science 18 (16) (1978) 1216–1219. doi:10.1002/pen.760181605.

[50] K. C. Sheth, Stress, mechanical and thermal characterization of anisotropic polyimide thin film and coatings, Ph.D. thesis, University of Massachusetts Amherst, Department of Polymer Science and Engineering (1996).

[51] D. Munoz-Martin, C. Brasz, Y. Chen, M. Morales, C. Arnold, C. Molpeceres, Laser-induced forward transfer of high-viscosity silver pastes, Applied Surface Science 366 (2016) 389–396. doi:10.1016/j.apsusc.2016.01.029.